Stratospheric gravity wave simulation over Greenland during 24 January 2005

Varavut Limpasuvan,[1] Dong L. Wu,[2] M. Joan Alexander,[3] Ming Xue,[4] Ming Hu,[4] Steven Pawson,[5] and James R. Perkins[6]

Received 24 July 2006; revised 10 February 2007; accepted 14 February 2007; published 24 May 2007.

[1] The "Advanced Regional Prediction System" forecast model is extended up to the stratopause and over the entire hemisphere to simulate gravity waves during 24 January 2005. With a 15-km horizontal resolution, the simulation produces dominant gravity wave features near Eastern Greenland that are associated mainly with orographic forcing by the Greenland terrain. The simulated wave temperature perturbations compare favorably with radiance perturbations from NASA Atmospheric Infrared Sounder observations. In the upper stratosphere (40–50 km), vertical overturning of the isentropes suggests the occurrence of wave breaking just east of Greenland that leads to a tremendous reduction of wave amplitudes. The associated flux divergence produces horizontal flow deceleration of 12–120 m s^{-1} day^{-1} and coincides with areas of depleted stratospheric wind speed, suggesting strong interactions between orographic gravity waves and the polar vortex. A simulation using the coarser 50-km horizontal resolution produces gravity waves of significantly weaker amplitudes.

Citation: Limpasuvan, V., D. L. Wu, M. Joan Alexander, M. Xue, M. Hu, S. Pawson, and J. R. Perkins (2007), Stratospheric gravity wave simulation over Greenland during 24 January 2005, *J. Geophys. Res.*, *112*, D10115, doi:10.1029/2006JD007823.

1. Introduction

[2] Wintertime meteorological conditions over the North Atlantic can foster strong stratospheric gravity waves during December and January. Intense surface flow over the terrain of Greenland, Scandinavia, and Svalbard can excite orographic gravity waves [e.g., *Leutbecher and Volkert*, 2000; *Doyle et al.*, 2005; *Eckermann et al.*, 2006]. When the prevailing wind exhibits small directional wind shear in the vertical across the tropopause, these waves propagate vertically well into the stratosphere. Flow conditions in this region can likewise emit inertia gravity waves because of imbalance of the jet stream. Where the horizontal jet is rapidly changing speed and direction, it can evolve (by adjusting the relationship between mass and velocity fields) through radiation of gravity waves [*Gill*, 1982]. *Buss et al.* [2004] reported inertia gravity waves in the stratosphere during January 2000 related to a stationary high mean sea level pressure ("blocking") and strong anticyclonic jet stream over the North Atlantic. Likewise, inertia gravity waves can result from synoptic-scale Rossby wave breaking related to the occlusion process of a maturing extratropical storm [*Hitchman et al.*, 2003] and persistent flow over the Scandinavian mountain ridge [*Dörnbrack et al.*, 2002]. Overall, these aforementioned studies report strong temperature perturbation (in the cold polar region) induced by these waves that can lead to the formation of polar stratospheric clouds (PSCs) in the lower stratosphere [*Carslaw et al.*, 1998, 1999].

[3] More recently, during the end of January 2005, extensive gravity wave activity was observed over the North Atlantic [e.g., *Maturilli and Dörnbrack*, 2006]. The predominant gravity wave features persisted on the eastern side of Greenland. The extent of their phase lines and wave amplitudes increased with altitude. Figure 1a shows strong radiance perturbations in the CO_2 15-micron emission band observed on 24 January 2005 by the Atmospheric Infrared Sounder (AIRS) aboard NASA AQUA satellite [*Aumann et al.*, 2003; *Fetzer et al.*, 2003]. The AIRS has a horizontal resolution of ~15 km. These perturbations are representative of gravity waves with vertical wavelengths in excess of 12 km that are resolved by the AIRS weighting function [*Alexander and Barnet*, 2006]. Using the mapping technique of *Wu and Zhang* [2004], the AIRS "background state" was first determined by fitting cross-(satellite)-track radiance with a third-order polynomial function. The fitted result was then smoothed along the satellite track with a 500-km running window (keeping features smaller than 500 km). The displayed radiance perturbations are defined as the difference between the observed radiance and this background.

[1]Department of Chemistry and Physics, Coastal Carolina University, Conway, South Carolina, USA.
[2]NASA Jet Propulsion Laboratory, California Institute of Technology, Pasadena, California, USA.
[3]Colorado Research Associate Division, NorthWest Research Associates, Inc., Boulder, Colorado, USA.
[4]Center for Analysis and Prediction of Storms, University of Oklahoma, Norman, Oklahoma, USA.
[5]Global Modeling and Assimilation Office, NASA Goddard Space Flight Center, Greenbelt, Maryland, USA.
[6]Department of Computer Sciences, Coastal Carolina University, Conway, South Carolina, USA.

Copyright 2007 by the American Geophysical Union.
0148-0227/07/2006JD007823

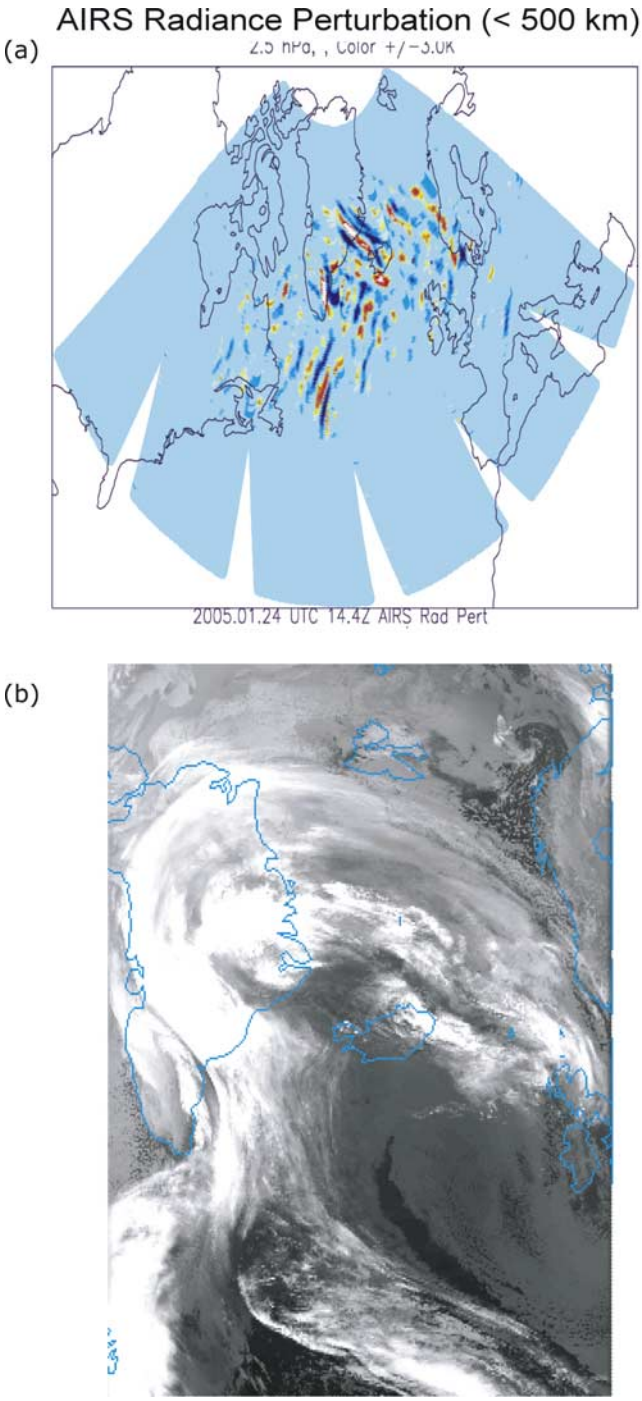

Figure 1. (a) AIRS observations (ascending orbits) at 2.5 hPa of radiance perturbations (of horizontal scales shorter than 500 km). The approximate equivalent temperature amplitude is noted in the subtitle. (b) Infrared image from the Defense Meteorological Satellite Program at 0913 UTC 24 January 2005.

[4] The particular 2004–2005 Arctic winter was unusual in that the polar vortex formed very early in the season and was very cold throughout [*Jimenez et al.*, 2006]. During 23–30 January 2005, the vortex was elongated in the upper stratosphere (stretching across North America and Northern Europe) and kidney shaped in the lower stratosphere (e.g., Figure 2). A strong anticyclone persisted over the Norwegian Sea that significantly raised the tropopause much like the conditions noted by *Buss et al.* [2004] and *Dörnbrack et al.* [2002]. The intense upper tropospheric flow over Southern Greenland was predominantly from the southeast (see Figure 1b). The lower stratosphere was the coldest on record. The observed region where PSCs could form ($T_{ice} < T < T_{NAT}$) was larger than any previous Northern Hemisphere winters [*Manney et al.*, 2006].

[5] Around the altitude of 18 km, this frigid region was identified mainly over the Svalbard Archipelago, between northeastern Greenland and Scandinavia. Indeed, on 26 January 2005, a lidar system over Norway's Ny-Alesund (Spitsbergen) and nearby balloon-borne water vapor measurements clearly observed stratospheric ice clouds [*Maturilli and Dörnbrack*, 2006] and severe water vapor depletion over Spitsbergen [*Jimenez et al.*, 2006]. Using mesoscale numerical simulations based on the Penn State/National Center for Atmospheric Research Mesoscale Model Version 5 (MM5) at 12-km horizontal resolution (with 4-km resolution nested grid) up to ~30 km in altitude, *Maturilli and Dörnbrack* [2006] demonstrated that temperature anomalies associated with orographic gravity waves (induced by the Svalbard terrains) caused significant cooling which accounted for the observed PSCs on January 26. These authors also noted the presence of inertia gravity waves [*Plougonven et al.*, 2003; *Plougonven and Snyder*, 2005] emitted spontaneously by the anticyclonic jet over the Norwegian Sea.

[6] The present paper focuses on this recent gravity wave activity observed over the vicinity of Greenland on 24 January 2005 during a remarkably cold winter. The study uses a compressible, nonhydrostatic weather prediction model that has been extended up to 56 km to simulate gravity waves throughout the stratosphere. To date, realistic modeling efforts cited above mostly extend up to a 30-km altitude. The wave occurrence is traced to its possible source in the troposphere, and wave dissipation in the upper stratosphere is diagnosed to estimate the wave influence on the polar vortex. Model simulation is tentatively compared with the AIRS observations and local soundings. The results suggest that the dominant gravity wave features near Eastern Greenland are associated mainly with orographic forcing by the Greenland terrain. During 0900–1100 Coordinated Universal Time (UTC), wave breaking is observed near Eastern Greenland between 40 and 50 km altitude layer, leading to local attenuation of wave amplitudes and strong deceleration of the prevailing flow.

2. Model Setup

[7] Developed at the University of Oklahoma Center for Analysis and Prediction of Storms, the "Advanced Regional Prediction Systems" (ARPS) [*Xue et al.*, 2000; 2001, 2003] version 5.0.0 is utilized for present numerical study. This finite difference, compressible, nonhydrostatic model is based on a generalized terrain-following coordinate system. The Jacobian matrix of transformation between the computational and physical grids is calculated numerically after the computational grid is defined. As such, the computational grid can be defined arbitrarily with allowance for stretching of the vertical grid spacing and the flattening of the upper level coordinate surfaces. The only requirement in

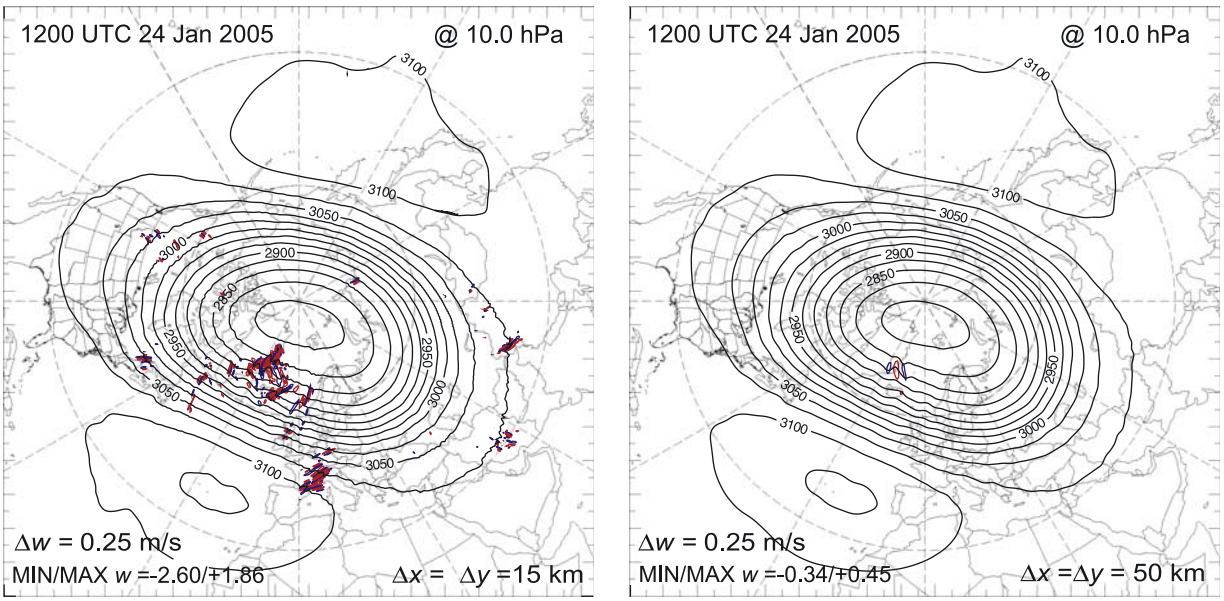

Figure 2. ARPS simulation at 1200 UTC 24 January 2005 and at 10 hPa. The geopotential height is given in black contours (every 25 dam). The vertical wind is given in color contours (every 0.25 m/s). Upward (downward) motion is shown in red (blue). Simulations from two different horizontal resolutions are shown, 15 km (left) and 50 km (right).

the ARPS grid generation is that the lowest grid level follows the terrain. In the present setup, unless specified otherwise, the ARPS model horizontal resolution is set to 15 km. The vertical grid spacing is specified to be about 20 m in the lowest level and gradually increases with altitude to 400 m at 12 km, above which the vertical grid spacing remains fixed at 400 m, and the coordinate surfaces are flattened.

[8] In general, the ARPS vertical coordinate setup differs from the MM5 used by, for example, *Wu and Zhang* [2004] and *Maturilli and Dörnbrack* [2006] for their simulations of gravity waves in the lower stratosphere (up to ~30 km). As described by *Dudhia* [1993] and *Grell et al.* [1995], the MM5 uses the standard sigma coordinate, on the basis of a static reference pressure profile and the pressure values at the model top and bottom, so the terrain-following vertical coordinate value ranges between 0 and 1. The MM5 transformation Jacobians are defined analytically and the coordinate surfaces do not go flat until the model top. In ARPS, while the lowest grid level conforms to the terrain, the vertical grid spacing can be varied freely. The flattening of the coordinate surfaces at the upper levels (well before the model top) reduces the errors associated with the calculation of horizontal gradients, such as the pressure gradient force terms, at those levels [*Xue et al.*, 2003].

[9] The bottom boundary condition is rigid and represents realistic terrain over the domain of the simulation. The global terrain height source is the 30 arc second US Geological Survey (Sioux Falls, South Dakota) data set (~0.920 km in latitude; ~0.920 km in longitude, weighted by the cosine of the corresponding latitude). A nine-point smoother is applied twice to the terrain after interpolating the height source to ARPS grid to significantly minimize forcing of motion near the unreliable model grid resolution limits.

[10] The ARPS uses the mode-splitting time integration technique of *Klemp and Wilhemson* [1978] to efficiently deal with sound (acoustic) waves (within the small time steps) typically present in a compressible model atmosphere. In present setup, the big time step integration (every 10 s) uses the leapfrog time differencing with a fourth-order centered advection scheme. In the small time step integration for acoustic modes, the time step size is 5 s. The Robert-Asselin time filtering with a coefficient of 0.05 is applied to the large time steps. To attenuate unstable sound waves that can be excited in the mode-splitting time integration [*Skamarock and Klemp*, 1992], an artificial three-dimensional divergence damping term with a nondimensional coefficient of 0.05 is included. The divergence damping has very little effects on meteorologically significant wave modes.

[11] All prognostic equations (except pressure) include fourth-order computational mixing to suppress small-scale computational noise and to control nonlinear instabilities. The horizontal and vertical computational mixing coefficients (scaled by the horizontal and vertical spacing, respectively) are both set to 10^{-4} s^{-1}. For subgrid-scale turbulence mixing (eddy diffusion), the 1.5-order turbulent-kinetic-energy-based scheme [e.g., *Deardorff*, 1980] is used. The formulations for these terms are given by *Xue et al.* [2000].

[12] Surface physics is turned on with surface fluxes (over land and water) computed using stability-dependent surface drag coefficient (diagnosed in the model) and predicted surface temperature and water content [*Businger et al.*, 1971; *Byun*, 1990]. The detailed calculation of the drag coefficient depends on the surface characteristics (soil types and vegetation data) which are obtained from the Global Ecosystems Database Version 1.0 from National Oceanic and Atmospheric Administration's National

Geophysical Data Center. A simple two-layer soil model, based on *Noilhan and Planton* [1989] scheme, predicts the ground surface temperature and soil moisture content.

[13] The microphysics scheme (with ice phase) of *Lin et al.* [1983] represents the model's moist processes. Cumulus convection is parameterized by the scheme of *Kain and Fritsch* [1993]. The combined usage of microphysics and cumulus convection parameterizations has been used successfully in similar medium-scale modeling of gravity waves [e.g., *Maturilli and Dörnbrack*, 2006]. A full radiative calculation is updated every 100 s. The treatment of shortwave and longwave radiation is based on the works of *Chou and Suarez* [1994] and *Chou and Suarez* [1999], respectively. A summary to the more recent updates to this radiation package can be found in the work by *Tao et al.* [2003].

[14] Global meteorological analyses are used to initialize the ARPS model. These data are from the NASA Goddard Earth Observation System, Version 4 (GEOS-4) analyses [*Bloom et al.*, 2005]. Every 6 hours, the GEOS-4 analyses are performed on a $1.25° \times 1.0°$ global longitude-latitude horizontal grid, extending from the surface to about 0.01 hPa. The GEOS-4 data are interpolated from isobaric surfaces onto the ARPS grid using a second-order polynomial and smoothed to minimize possible near-grid-scale noise introduced by the interpolation. The interpolated wind fields are then adjusted to maintain the anelastic mass continuity which has been found to reduce initial pressure oscillations.

[15] Initially, the simulation is run in a hemispheric mode (HM), centered over the Northern Hemisphere polar cap (1171×1171 grid points) using the polar stereographic map projection, with a rigid top boundary condition set at 38 km (93 vertical levels). This initial run surveys possible gravity wave activity over the northern hemisphere up to the lower stratosphere during 24 January 2005. To examine gravity waves up to the stratopause while keeping the simulation within our available computing resources, the second simulation is run in a regional mode (RM) of 8900- $\times$ 7200-km horizontal domain (595×483 grid points), with a rigid lid at 56 km (in all, 143 levels). This latter run focuses on areas where identifiable wave activity appears in the HM mode (see also section 3.1). For this regional setup, the simulation is nested (via one-way interaction) with a coarser external, time-dependent lateral boundary condition provided by the GEOS-4 reanalysis data. Relaxation (at a rate of 0.002 s^{-1}) toward the external field is imposed in a 200-km-wide zone near the lateral boundaries to reduce potentially large inconsistencies between the model solution and the external GEOS-4 data [*Davies*, 1983].

[16] In all simulations, the upper level Rayleigh damping becomes effective at the vertical level of 32 km for HM and 50 km for RM. The inverse of the *e*-folding timescale of damping at the model top is set to 0.033 s^{-1} for all runs. This damping strictly serves to prevent spurious wave reflection from the rigid top boundary. All results presented here in planar and cross-sectional views are well below this layer and are therefore unaffected by the imposed damping. Results are saved every 6 min of simulation time.

[17] In the ARPS, state variables and wind components are divided to two parts, their "base state" and their deviations from the base state. The base state is assumed to be time invariant, hydrostatically balanced, and homogeneous in the horizontal. Here, in using the GEOS-4 as the initial data set, the base state is constructed as the horizontal domain average of state variables and wind components, with the pressure derived from the hydrostatic relationship.

[18] The ability of the ARPS model in simulating orographically forced flows has been rather thoroughly tested in the work of *Xue et al.* [2000] for idealized mountains of various spatial scales and for real terrain in reproducing intense downslope wind storms. In the work of *Doyle et al.* [2000], the ability of the ARPS model in reproducing the 11 January 1972 downslope windstorm over the Grand Junction (Colorado) was further demonstrated through intercomparisons with a number of other mesoscale models. More recently, *Chow et al.* [2006] report on successful high-resolution simulations of detailed flows within a deep valley, which were both dynamically and thermally forced. *Horinouchi et al.* [2002] successfully extended the ARPS up to the thermopause to study convectively generated gravity waves propagating into the middle atmosphere. Idealized terrain was used in that study with a much smaller horizontal domain and periodic horizontal boundaries and a single sounding to describe the initial vertical variations. Excited gravity waves in the simulation were seen to break above the upper mesosphere, producing features often observed in airglow imaging.

3. Results

3.1. Planar View

[19] The left panel of Figure 2 shows a sample result of the HM simulation at 15-km horizontal resolution, valid at 1200 UTC, 24 January 2005 (i.e., 12 hours after initialization). At 10 hPa, a well-defined polar vortex low is displaced slightly off the pole, with adjacent high geopotential height centers over the northern ocean regions. Strong vertical velocities, with alternating bands of upward and downward motion, are present in association with gravity waves over the North Atlantic. For the simulation with a lower 50-km horizontal resolution (right panel of Figure 2), a similar height field is shown. However, throughout the hemisphere, gravity waves are nearly absent in terms of the vertical velocity, when presented at the same contour interval. As noted by *Leutbecher and Volkert* [2000], the increase in horizontal resolution results in larger stratospheric gravity wave amplitude by better resolving shorter waves as well as orographic forcing.

[20] To examine the North Atlantic gravity wave features at higher altitude, a RM simulation with 15-km horizontal resolution is performed for the domain centered over the southern tip of Greenland. For this mode, the imposed Rayleigh damping becomes effective above 50 km. Figure 3 demonstrates that the ARPS simulation of 300 hPa height and wind speed compares very well with the GEOS-4 reanalysis at the same time (Figures 3b and 3c; and later comparison of soundings in Figure 6). A ridge is situated over the North Atlantic (just off the coastline of Northern Europe; see also Figure 1b) adjacent to an elongated deep trough over eastern Canada. Relative to the initial condition (0000 UTC), the simulated jet flow (Figure 3c) over Greenland has migrated northward with a more pronounced anticyclonic curvature on the western side over Greenland at 1800 UTC than in the GEOS-4 data (Figure 3b). The modeled flow, at

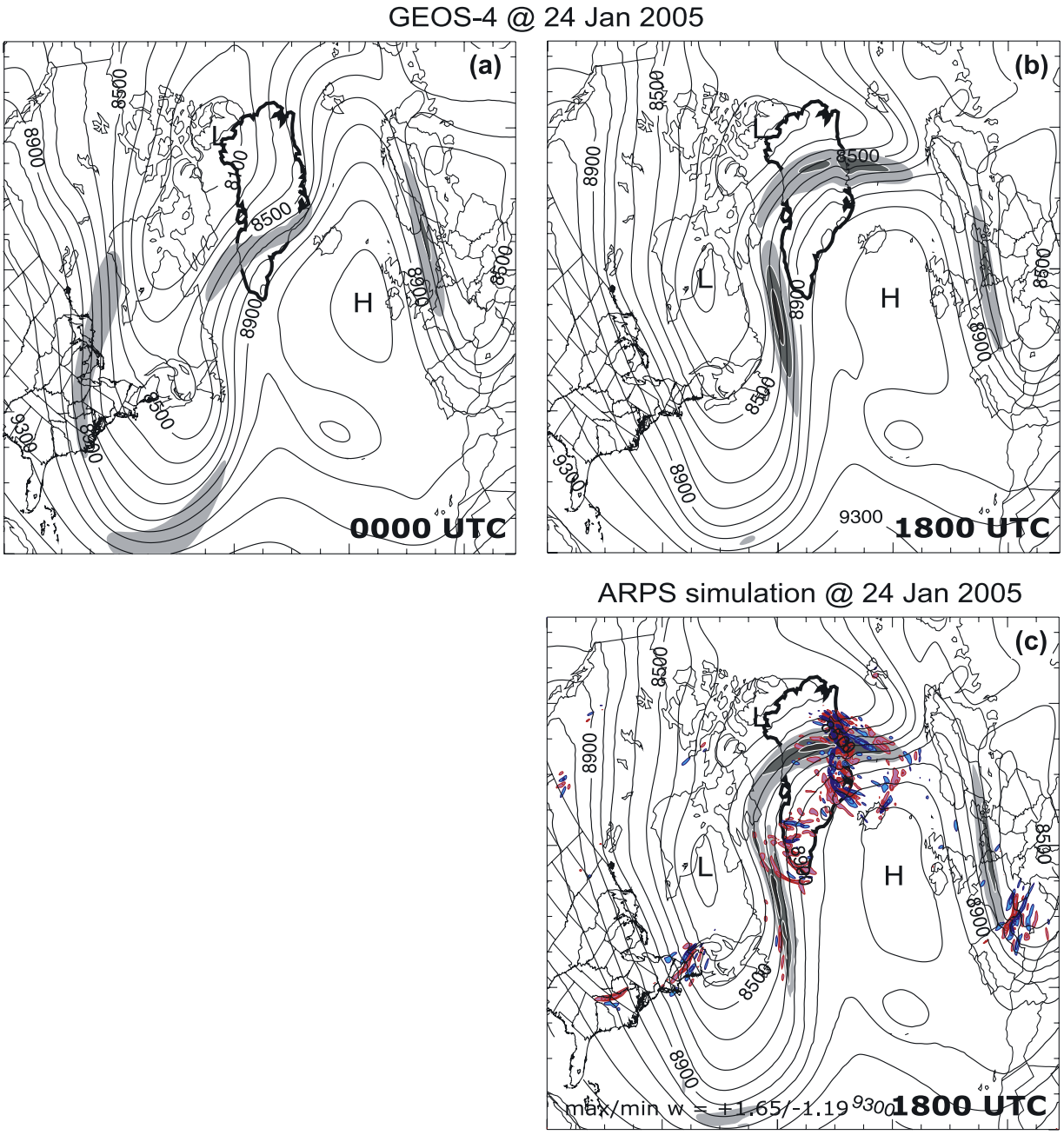

Figure 3. (a) GEOS-4 data at 0000 UTC of 24 January 2005 (initial condition). The 300-hPa geopotential height is given in black contours (every 100 m). Shaded regions show areas where the 300-hPa horizontal wind speed exceeds 60, 70, 80 m/s (darkest). (b) Same as Figure 3a except at 1800 UTC. (c) Same as Figure 3a except for the ARPS simulation at 1800 UTC (initialized with 0000 UTC GEOS-4 data). The 80-hPa vertical wind is given in filled color contours (every 0.1 m/s). Upward (downward) motion is shown in red (blue). Greenland is outlined in heavy black line.

this higher resolution, has also strengthened more during this period with horizontal wind speed exceeding 80 m/s over Greenland and the Labrador Sea. The simulated vertical velocities at 80 hPa (superimposed on the 300 hPa fields as blue/red contours on Figure 3c) are consistent with the perturbations shown in Figure 2 over the North Atlantic and akin to features observed by AIRS (Figure 1a). In particular, the strongest wave activities are found along central eastern Greenland and the southern portion of the western Greenland, suggesting the important role of forcing by the coastal terrain.

[21] Figure 4 shows the simulated tropospheric conditions (200 and 500 hPa levels) at 6 and 18 hours after initialization. South of Greenland, a strong upper tropospheric front exists over the mid-Atlantic with strong temperature gradient (green contours) and intense bands of midtropospheric upward motion (red-filled contours). As time progresses, the frontal structure weakens and the upper level jet exhibits

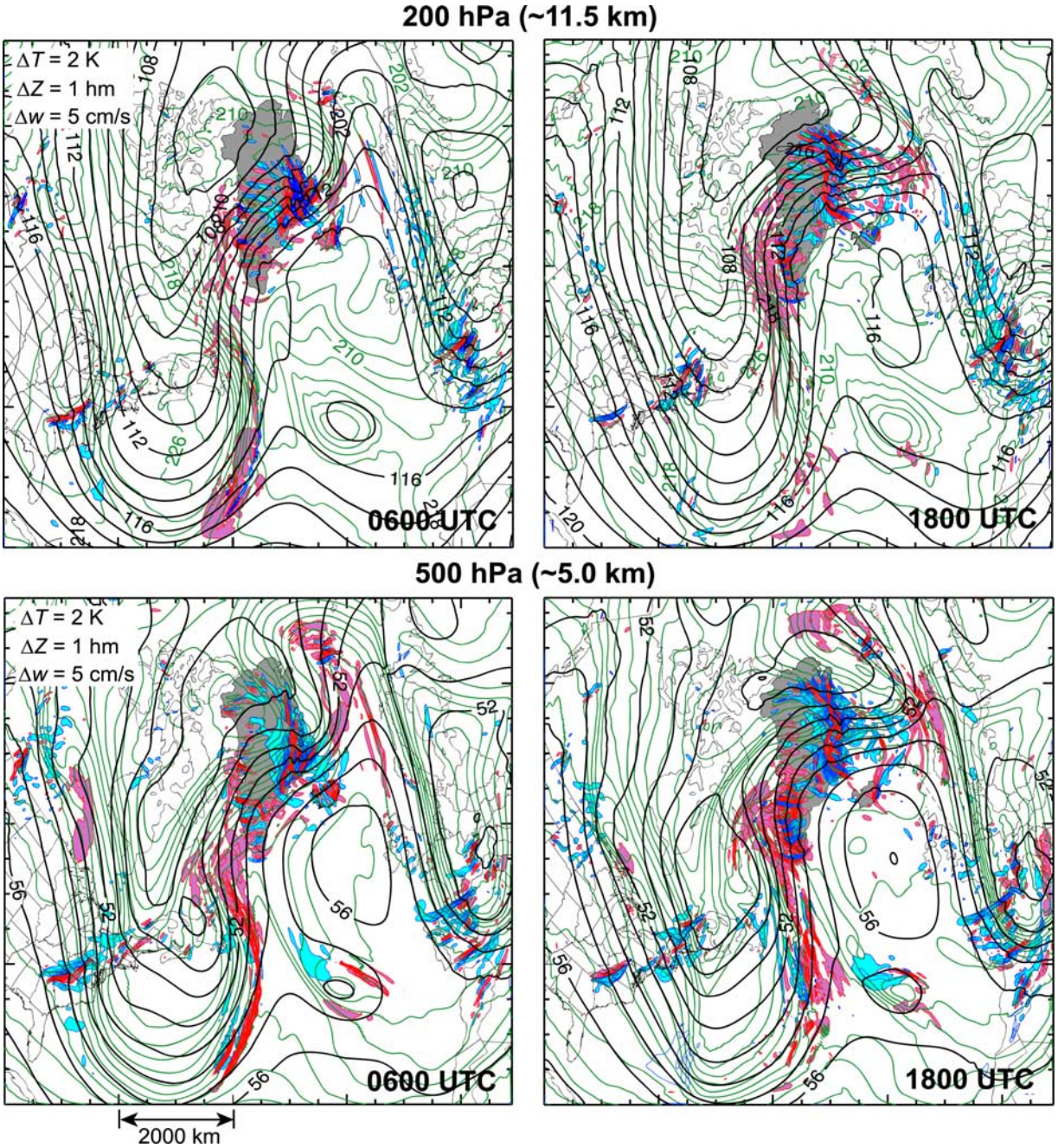

Figure 4. (Top row) ARPS simulations at 0600 UTC and 1800 UTC of 24 January 2005 and at 200 hPa. The height field (Z, in hectometer) and temperature field (T, in Kelvin) are given as black and green contours, respectively. The vertical wind (w) is given as filled color contours; upward (downward) motion is shown in red (blue). Contour intervals are indicated. (Bottom row) As above except at 500 hPa. Greenland and Iceland are shaded in gray.

more anticyclonic curvature near Greenland (see also Figure 3). The synoptic conditions in this time frame are further described by *Maturilli and Dörnbrack* [2006]. In their observations and simulation of gravity waves during 13–14 January 2000, *Buss et al.* [2004] reported very similar troposphere conditions as shown in Figure 4 (see their Figure 3).

[22] Figure 5 demonstrates the same fields as Figure 4 but in the stratosphere at the 2.5 hPa (~40 km) and 50 hPa (~20 km) levels. The strong ridge observed over the North Atlantic in Figure 4 is still evident at 50 hPa because of the elevated tropopause and anticyclone. As a result, the lower stratospheric flow (~20 km) tends to be oriented in the same direction as the tropospheric jet around Greenland, favoring upward gravity wave propagation (see also Eastern Greenland and Iceland wind profiles in Figure 6). Similar prevailing flow structure over central Greenland was also noted by *Buss et al.* [2004]. In the upper stratosphere (2.5 hPa), the flow is predominantly circumpolar, but the vortex is slightly displaced toward Greenland (see also

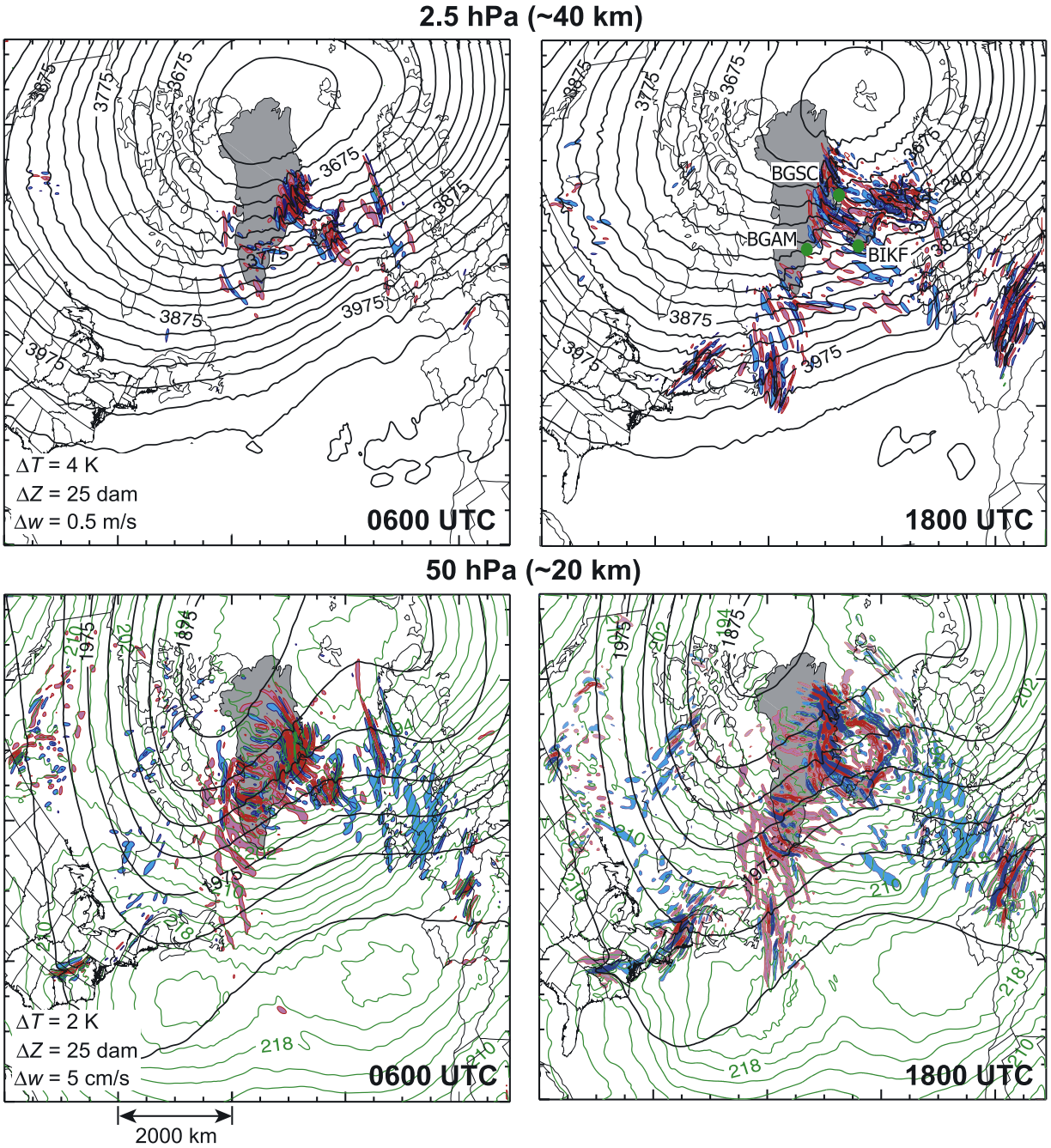

Figure 5. Same as Figure 4 except at 2.5 and 50 hPa. Z is in decameter. For the 2.5-hPa diagram, the temperature contours are omitted for clarity. Green dots locate the observational stations at Tasiilaq (BGAM) and Ittoqqortoormiit (BGSC) on Eastern Greenland and at Keflavikurflugvollur (BIKF) on Iceland. Greenland and Iceland are shaded in gray.

Figure 2). The flow over the eastern Greenland coast is predominantly eastward at 1800 UTC (and at other times as shown, for example, in Figure 6 at BGSC).

[23] Clusters of enhanced vertical velocity perturbations (filled color contours) are present near or downstream of the Appalachians Mountain, Greenland, and the Pyrenees. In particular, wind perturbations associated with the Appalachians appear in two separate patches of wave activity, one over the Virginia Appalachians and another north of Maine. However, the predominant vertical velocity perturbations throughout the troposphere and stratosphere are those over much of eastern Greenland (where the flow tends to align at different levels). While relatively weak (with magnitude less than 2 m/s) at 80 hPa, vertical velocity fluctuations are much stronger at higher altitude as a result of amplitude amplification due to reduced atmospheric density.

3.2. Comparison With Observations

[24] Local station soundings are compared with those extracted from the RM simulation. Figure 6 shows temper-

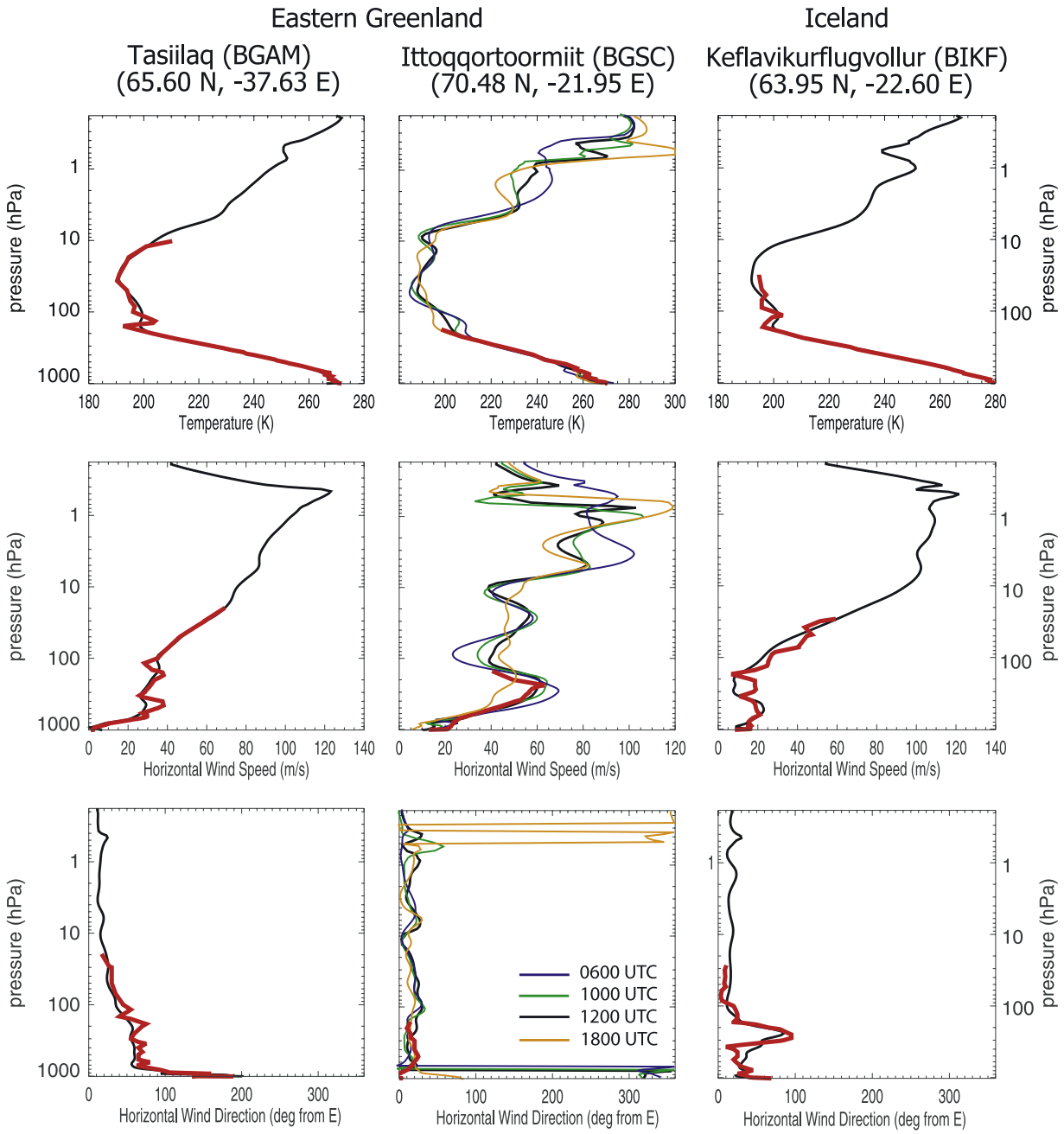

Figure 6. Soundings at Eastern Greenland (stations BGAM and BGSC) and Iceland (station BIKF) during 12 UTC 24 January 2005. The locations of these stations are shown in Figure 5. Model (observational) data are shown in thick black (red) line. For BGSC, model profiles during other times are also shown to illustrate wind and temperature evolution prior to and after 18 UTC.

ature and horizontal wind profiles on 24 January 2005 for two Eastern Greenland locations (Tasiilaq and Ittoqqortoormiit) and at Keflavikurflugvoluur (Iceland). The locations of these stations are marked in Figure 5 (top). The model profiles at the station locations are linearly interpolated from the four neighboring grid points. At 1200 UTC, a good general agreement is found between the simulated profiles and actual observations throughout the troposphere and up to highest observed levels (compare the red and black profiles). The observed profiles have more vertical variations than in the simulation which may be due to the smoothing nature of linear interpolation used in extracting the simulated profiles. Comparisons at other locations in Greenland and the Svalbard (Norway) at 1200 UTC are also favorable (not shown). Overall sounding comparisons suggest that the model is simulating the basic flow and thermal structures well below 20 hPa. The more transient and fine-scale gravity wave features that develop in the simulation may therefore be plausible.

[25] As noted in Figure 1a, gravity waves over Greenland were observed by AIRS on 24 January 2005. Similar gravity wave features are simulated in the model in the same

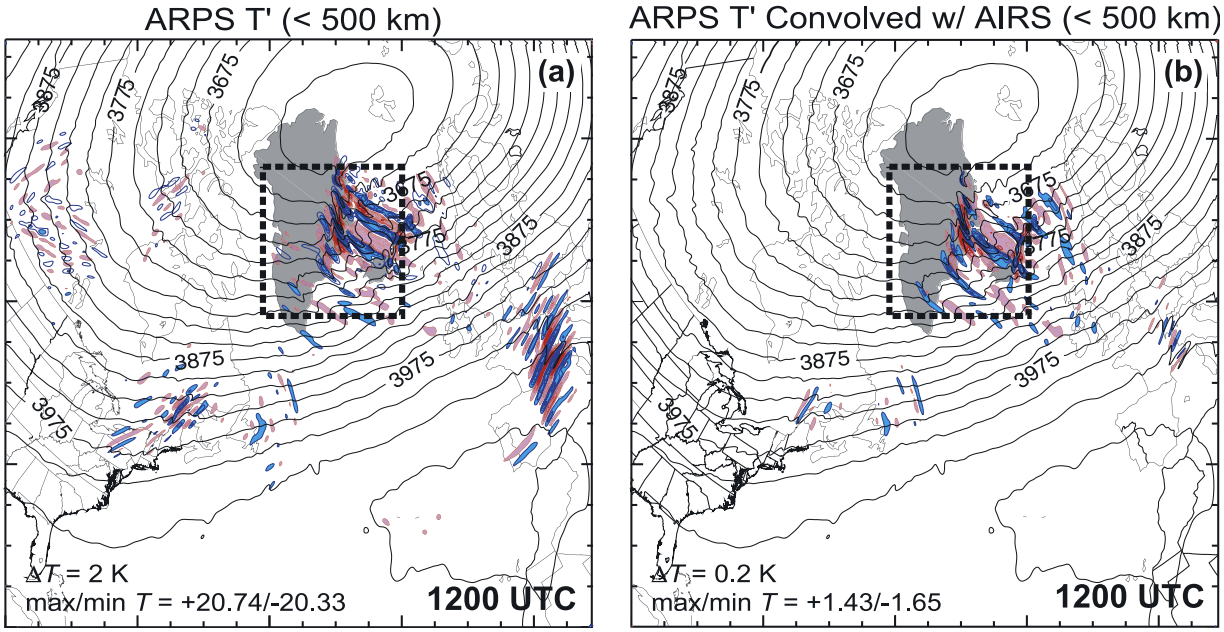

Figure 7. (a) 1200 UTC ARPS temperature (T) perturbations simulation at 2.5 hPa (contour interval indicated). Positive (negative) perturbation is shown in red (blue). The perturbation is defined as the difference between the temperature simulation at 1200 UTC and the simulation's basic state (time independent base-state of the model). The geopotential height is given in black contours (every 25 dam). Temperature perturbations of horizontal scale greater than 500 km have been removed. (b) Same as Figure 7a except the perturbations had been convolved with the weighting function of the 667.77 cm^{-1} AIRS channel. The rectangular box indicates the region of focus in the subsequent figures. Greenland and Iceland are shaded in gray.

vicinity (Figure 5). However, to compare with AIRS observations, the modeled temperature perturbations must be convolved (blended) with the broad vertical AIRS weighting functions (corresponding to the 15-micron band). The convolution process reduces wave amplitudes substantially. Figure 7b shows the simulated 2.5-hPa temperature perturbations convolved with the weighting function of the 667.77 cm^{-1} AIRS channel, which peaks near 2.5 hPa. As AIRS vertical coverage extends higher than the current model level, climatological temperature values from Cooperative Institute for Research in the Atmosphere [*Fleming et al.*, 1990] are used to extend the model result to the upper limit of the AIRS weighting function before convolution. While the convolved perturbation temperature is greatly diminished from the actual model output (compare Figures 7a and 7b), the overall structure shows likeness to the AIRS observation around the same time period, particularly the geolocation of wave oscillations near Eastern Greenland (as highlighted in rectangular boxes shown in Figure 7). As the visibility limit of AIRS weighting function is ~12 km in vertical wavelength, gravity waves with shorter vertical wavelength (and of slower vertical group velocity) are not well detected by AIRS [*Alexander and Barnet*, 2006]. This is why the convolved perturbations over the Pyrenees are much reduced in amplitudes.

[26] Notable differences between AIRS and the simulation are clearly present. As seen in Figure 1a, the AIRS data identified quite energetic gravity waves over southern Greenland and over the Atlantic. These features are nearly absent in the ARPS simulations. Additionally, the ARPS data wave characteristics appear nearly monochromatic while the AIRS fluctuations show some cross-hatched phase structures because of the superposition of different wave phase fronts. Finally, the AIRS brightness temperature amplitudes (±3 K) are much larger than the ARPS amplitudes.

[27] These differences may be attributable to the intermittency of gravity waves and the time sampling of the AIRS observations. In Figure 1a, adjacent AIRS swaths are separated by 90 min, while the ARPS results are instantaneous at 12 UTC of 24 January 2005. Features that are short-lived may be present in previous AIRS swaths (and plotted) and yet absent in ARPS. Furthermore, in plotting Figure 1a, the AIRS swaths are overlapped at high latitudes as AQUA's orbit drifts westward. The swaths on the western side are simply plotted over the eastern side ones, without grid averaging. The overlapping of swaths can contribute to the apparent superposition of AIRS phase fronts not present in ARPS or reality.

3.3. Focus on Eastern Greenland: Wave breaking

[28] Figure 8 shows the evolution of the 2.5-hPa wave perturbations in the rectangular box drawn on Figure 7. This is essentially a close-up view of Figure 5 (top row). Up until 0600 UTC, the perturbations over Eastern Greenland and Iceland grow in amplitude and spatial extent. Where the perturbations are pronounced (near the AB line segment), the nodal lines (zero vertical velocity; unfilled black contours) tend to tilt southward toward the east and remain nearly fixed in location, as shown in Figure 8 at 0600 UTC. Along the AB line, the horizontal wavelength is 80–300 km.

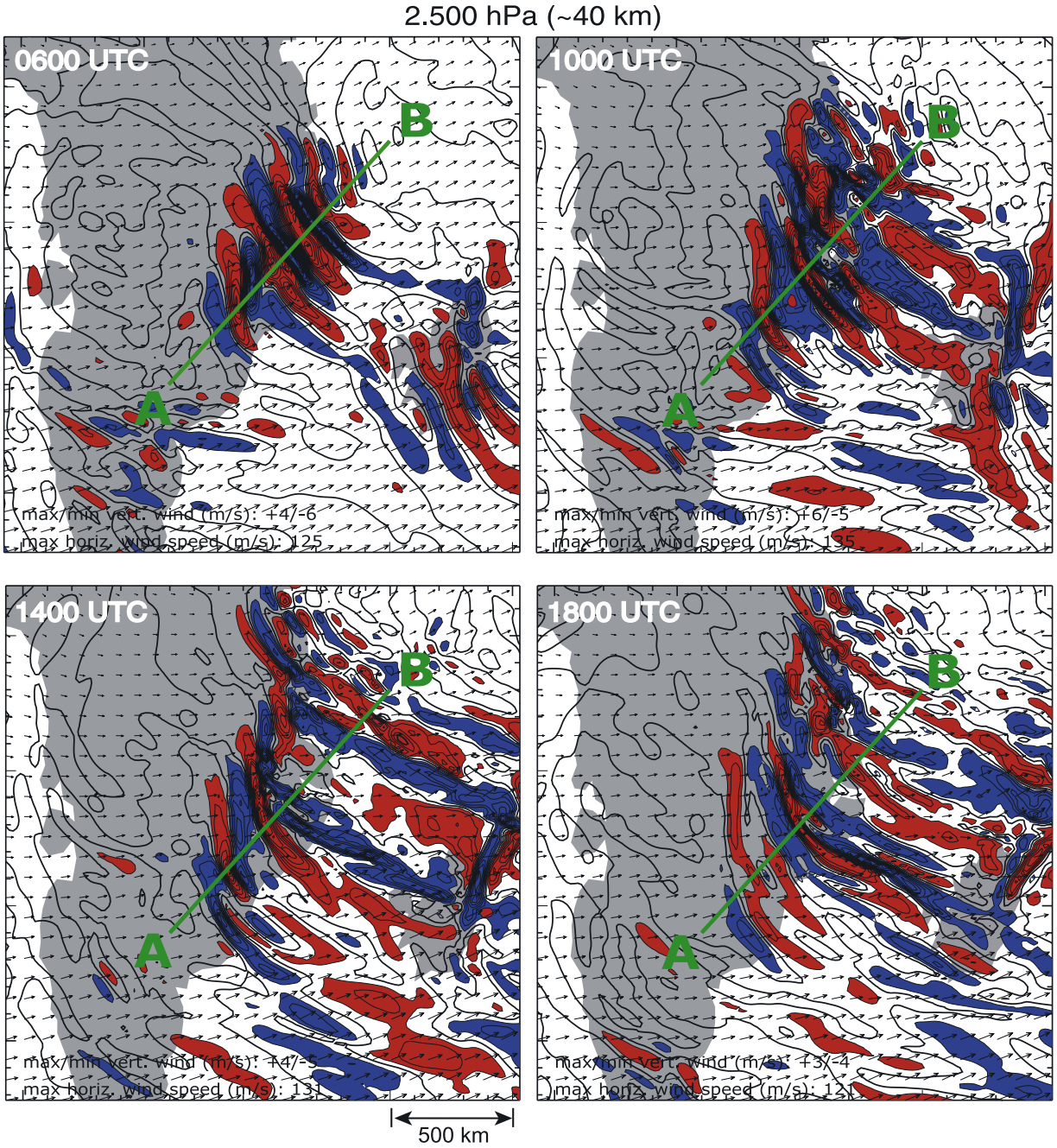

Figure 8. Evolution of the simulated 2.5-hPa vertical velocity every 4 hours in the rectangular region box shown in Figure 7. Positive (negative) perturbation is shown in red (blue). Contour level is 0.5 m/s. The black contour indicates zero vertical velocity. Greenland and Iceland are shaded in gray. Vectors show the horizontal wind. Green line shows the AB slice used in subsequent figures.

Horizontal wind vectors tend to be normal with respect to the phase lines.

[29] After 0600 UTC, wave perturbations from Eastern Greenland extend across the Greenland Sea (between Greenland and Iceland) with bow-like phase lines, concaved toward B. This "bow-like" characteristic is similar to the orographic gravity waves generated by near-surface flow over an isolated, three-dimensional ridge [e.g., *Nappo*, 2002]. Perturbations over Iceland begin to interfere with this growing wave pattern, resulting in eastward-pointing wavefront over northeastern Iceland. By 1400 UTC, the perturbations along AB still remain nearly stationary. However, the wave amplitudes have greatly diminished and the wave structures, particularly just eastward of the northern segment of the AB line, have deteriorated. For example, a void in the color-filled contours is evident, showing the Greenland continent and surface below. By 1800 UTC, this void is again replenished by wave perturbations over the Greenland Sea.

[30] The vertical cross-sections at AB line are shown in Figure 9. The left-hand side of Figure 9 illustrates the flow above 8 km. Consistent with Figure 8, at 0500 and

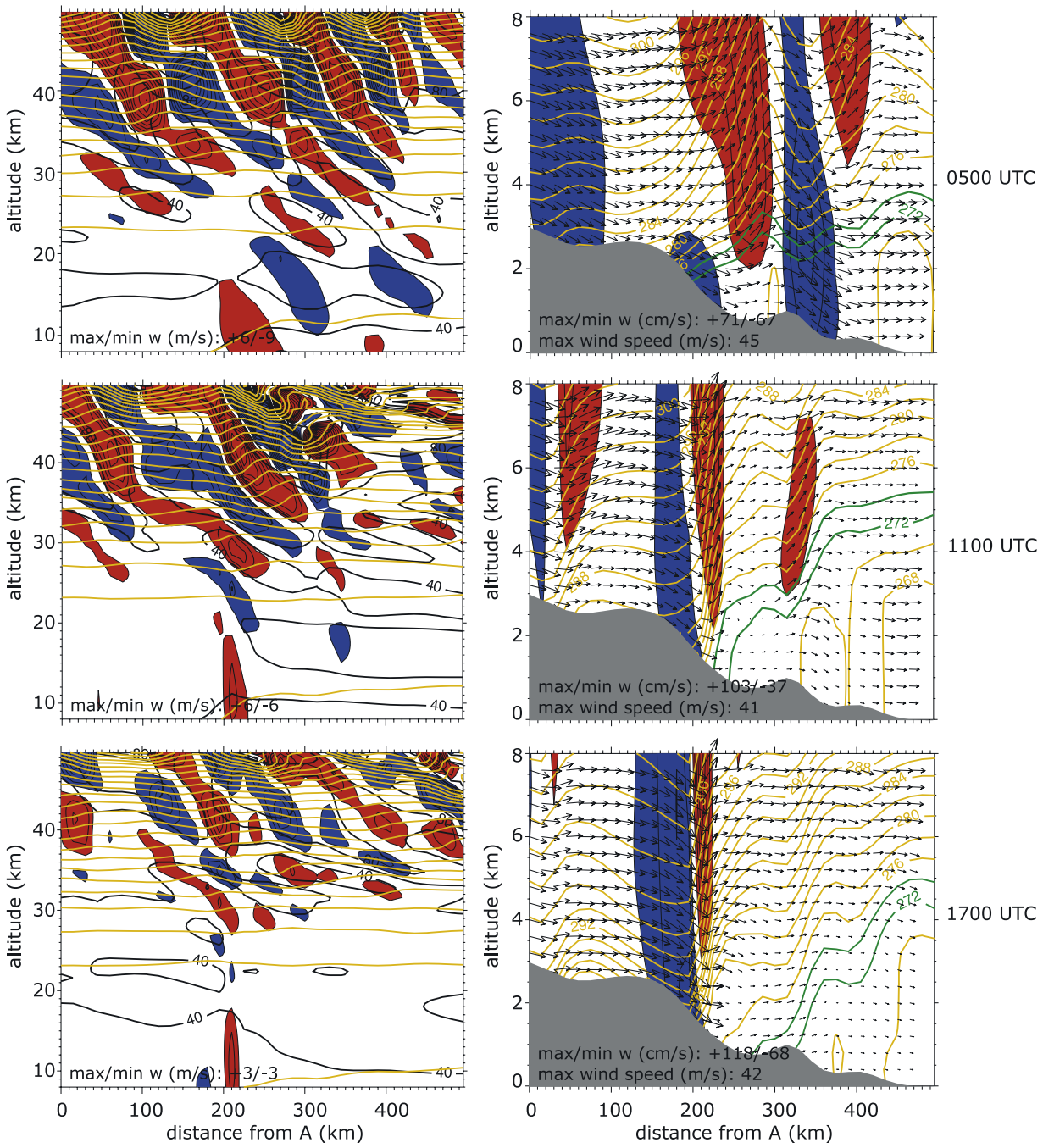

Figure 9. AB slice vertical cross-sections at every 6 hours of simulation. The left (right) diagram mainly covers the atmosphere above (below) 8 km. The vertical wind is shown as filled color contours (left, every 0.5 m/s; right, every 20 cm/s). The potential temperature is shown in orange contours (left, every 100 K; right, every 2 K). Green contours highlight the 272–274 K layer. The total horizontal wind speed is given as black contours (every 20 m/s) on the left panel. Cross-sectional wind is shown as vectors on the right. The Eastern Greenland terrain is shown in gray.

1100 UTC, the wave phase pattern is relatively stationary in time. As the AB section is nearly parallel the prevailing flow above 10 km (see Figures 5 and 6), the wave phase lines tilt upstream with altitude (toward A) into the wind. The overlaid isentropes (orange contours) are highly perturbed. Local extrema of potential temperature values are in quadrature with the vertical velocities. The horizontal wind speed (black contours) below 10 hPa is between 40–60 m/s, while above it can exceed 120 m/s. Such variation in wind speed presumably causes the wave vertical wavelength to range between 7 and 20 km [e.g., *Eckermann and Preuesse*, 1999].

[31] During 1100 UTC, the vertical gradient of potential temperature above 40 and 300 km from A reverses sign. The isentropes exhibit an "S" shape (becoming more vertical) indicative of the overturning of material surfaces and wave breaking, as the wave amplitudes experience

tremendous growth. This breaking process is followed by the aforementioned void in the wave packet pattern observed in Figure 8 at 1400 UTC near the middle of the AB segment. Thereafter, the wave amplitude and prevailing flow speed are significantly reduced. At 1800 UTC (Figure 9), the stratospheric flow speed and maximum vertical velocity is now 105 and 3 m/s, respectively, as compared with 140 and 9 m/s during 0500 UTC (see also Figure 8).

[32] The right-hand side of Figure 9 illustrates the flow evolution below 8 km. Persistent flow down the Eastern Greenland terrain slope can have speed of ~20–30 m/s and is accompanied by large vertical velocity perturbations. The extended terrain downslope in the middle of the AB segment can induce perturbations that penetrate across the tropopause (left Figure 9; note the difference in vertical velocity contour intervals). Because of the prevailing flow down the Greenland slope, the isentropes (as highlighted in green) migrate to the right as time increases.

[33] Together, Figures 8 and 9 suggest that the perturbations over Eastern Greenland are associated with orographic gravity waves. The wave cross-sectional structure is similar to those predicted by previous numerical studies of gravity waves generated by an isolated mountain ridge [e.g., *Xue and Thorpe*, 1991; *Xue et al.*, 2000; *Nappo*, 2002]. The wave phase tilting upstream with altitude (toward A) into the wind is consistent with upward and upwind energy propagation of orographic gravity waves [*Smith*, 1979]. Likewise, the wave phase patterns are nearly stationary in time (except possibly when wave breaking is occurring). Orographic gravity waves require relatively strong low-level flow. Here it is 20–30 m/s and strongest over the slopes. On the lee slope, orographic gravity waves are particularly pronounced at 1700 UTC (Figure 9). Overall, the pattern of the simulated isentropes is similar to previous reports on strong downslope wind storms [e.g., *Lilly and Zipser*, 1972; *Xue et al.*, 2000]. In the current case, the excited waves do not appear to be strong enough to cause isentrope overturning in the lower troposphere. Hence the resulting gravity waves propagate to the upper levels. Downslope flow at Grand Junction (Colorado) simulated by *Xue et al.* [2000] and over Antarctica by *Watanabe et al.* [2006] indeed generated orographic gravity waves that reached the stratosphere.

[34] Given the horizontal wavelength of 80–300 km along the AB line (shown in Figure 8), the linear gravity wave dispersion relationship can be used to predict the vertical wavelength [*Fritts and Alexander*, 2003]. For the buoyancy frequency (N) of ~0.02 s^{-1}, background stratospheric wind speed (both of which can be inferred from Figure 6), and the zero ground relative frequency of orographic gravity waves, the vertical wavelength (for such horizontal scale) should be 8–17 km between the tropopause and 44-km altitude. This prediction is within the vertical wavelength range noted in the AB cross-sections (Figure 9). Above 44 km where the wave amplitude and background wind speed can be quite large, linear theory suggests a much larger vertical wavelength (30–45 km) than actually present in the simulation. This discrepancy may be due to the failure of linear approximation at this altitude range where wave breaking and secondary wave generation from the breaking regions can occur. Some errors in the linear theory calculation are also likely because of the horizontal and temporal variations that occur in both the wind and wavefields.

[35] We note that strong anticyclonic jet with pronounced curvature anticyclonic flow (over the Norwegian Sea) in our simulation (Figures 3, 4, and 5) can potentially radiate inertia gravity waves as a result of flow imbalance [*Plougonven et al.*, 2003; *Buss et al.*, 2004; *Plougonven and Snyder*, 2005]. In fact, the present anticyclonic tropospheric flow strongly resembles the flow described by *Buss et al.* [2004] in their gravity wave study of 14 January 2000. In that case, these authors diagnosed inertia gravity waves over the northern part of Eastern Greenland and orographic gravity waves over the central part of Eastern Greenland (see their Figures 4 and 8). Furthermore, *Maturilli and Dörnbrack* [2006] noted gravity wave features over Spitsbergen during 26 January 2005 to be inertia gravity waves radiating away from the jet core that were followed by the presence of orographic gravity waves. During this transition, the local wavefronts that were initially parallel to the jet become perpendicular to the flow.

[36] In the present case, while jet imbalance (and subsequent emission of inertia gravity waves) may also be present in our RM domain, wave perturbations over Eastern Greenland (shown in Figures 8 and 9) appear to be mainly topographically forced. The presence of strong surface winds across the terrain orientation provides the near-surface source. In the work of *Buss et al.* [2004], despite the high elevation of the northern part of Eastern Greenland terrain, orographic gravity waves were absent above 200 hPa because of the strong change in the background wind direction with altitude (more than 90°) and the existence of a critical layer for stationary waves (see their Figure 6). These conditions led to wave absorption that inhibits orographic gravity wave propagation into the stratosphere. In our simulation, these conditions are not present. Near the center of the wave packet shown in Figure 8 (for example, at Ittoqqortoormiit, Greenland), wind profiles clearly demonstrate that the prevailing flow above the tropopause was constantly toward the east with speed in excess of 20 m/s. Therefore simulated gravity waves generated near the surface by orography can readily reach the upper stratosphere as seen in Figure 9.

3.4. Wave Forcing of the Larger-Scale Flow

[37] Linear wave theory predicts that mountain wave amplitude is proportional to the near-surface wind speed in the direction of terrain height gradient as well as to the terrain height. Mountain waves can readily propagate upward when the lower tropospheric flow, the upper tropospheric jet, and the stratospheric jet are all aligned in the same direction [*Smith*, 1979]. Upon reaching higher altitudes, wave breaking can occur and impose a strong decelerative effect on the jet. Wave breaking appears where wave amplitudes are large (as result of density decreasing rapidly with elevation) and/or where wind shear refracts the waves to short vertical wavelength.

[38] As shown in Figures 4, 5, and 6, the Eastern Greenland coastal region is located where the prevailing flow tends to align (predominantly eastward) throughout the atmosphere. For example, at station BGSC where the upper level gravity wave activity is the strongest (c.f., Figure 5), the horizontal

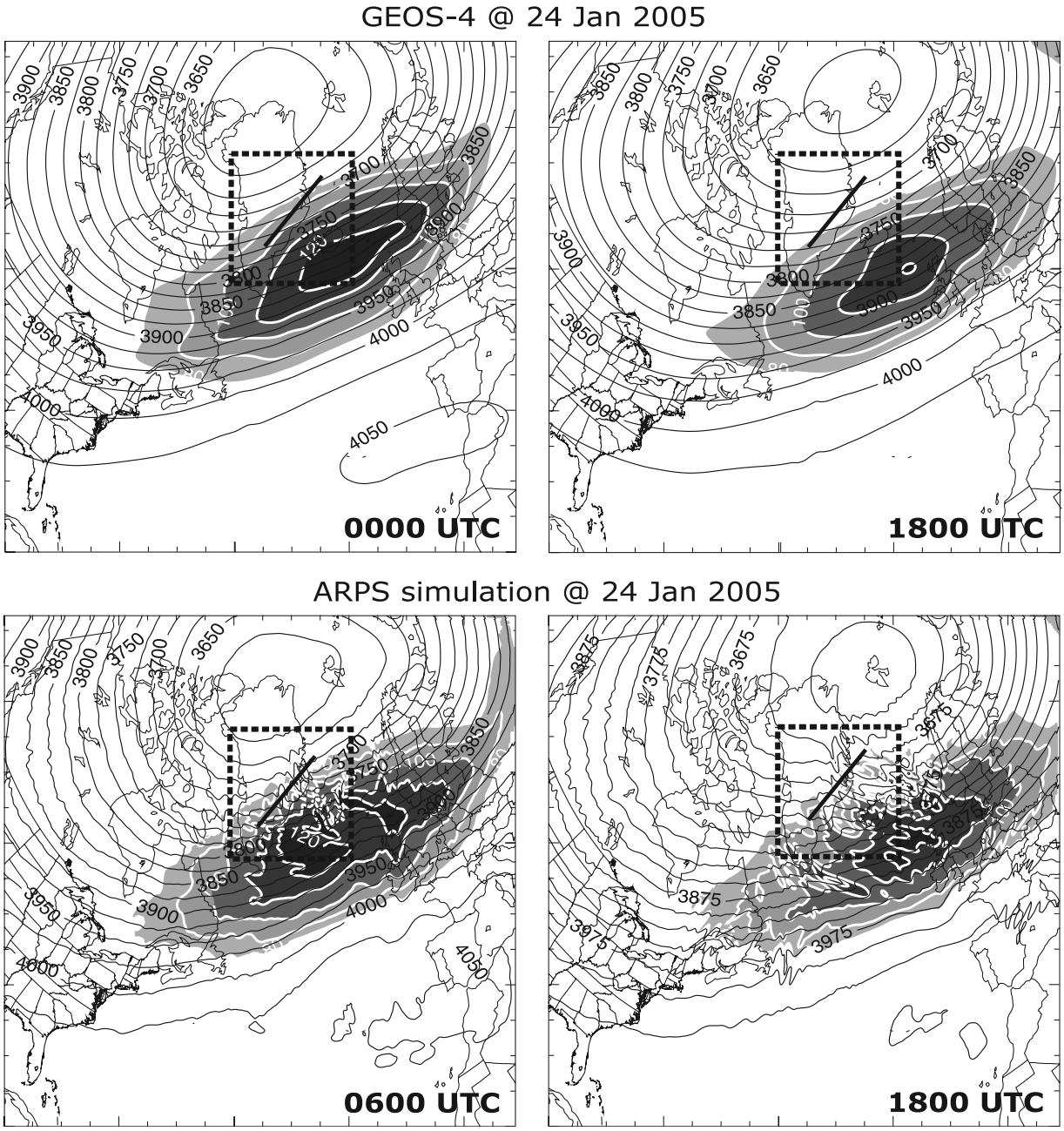

Figure 10. (Top row) GEOS-4 data at 0000 UTC (initial condition) and 1800 UTC of 24 January 2005. (Bottom row) ARPS simulation at 0600 UTC and 1800 UTC (initialized with 00 Z GEOS-4 data). The 2.5-hPa geopotential height is given in black contours (every 25 dam). Shaded regions show areas where the 2.5-hPa horizontal wind speed exceeds 80, 90, 100, 110, and 120 m/s (darkest). The thick line over Eastern Greenland indicates the AB slice and is shown for reference. The rectangular box indicates the region of focus shown in previous figures.

wind is almost entirely unidirectional throughout the depth of the atmosphere (Figure 6), and the near surface winds are also stronger than at the other two stations (Figure 6). Such condition favors upward propagation of gravity waves forced by the strong flow over topography. When these waves reach the upper stratosphere, the tremendous wave growth (due to the much decreased density) eventually leads to wave breaking as seen in Figure 9. Because the vertical alignment of horizontal wind tends to be found in the inner core of the polar vortex, as in this case near Eastern Greenland, the domain focused in Figure 8 (the boxed region in Figure 7) exhibits the strongest orographic forcing.

[39] Figure 10 illustrates the changes in the horizontal wind speeds at 2.5 hPa with respect to the initial condition. In comparing the 1800 UTC GEOS-4 data with that of the simulation, it appears that, while the overall large scale flow has weakened in time, perturbations associated with orographic gravity waves (and eventual wave breaking) tend to

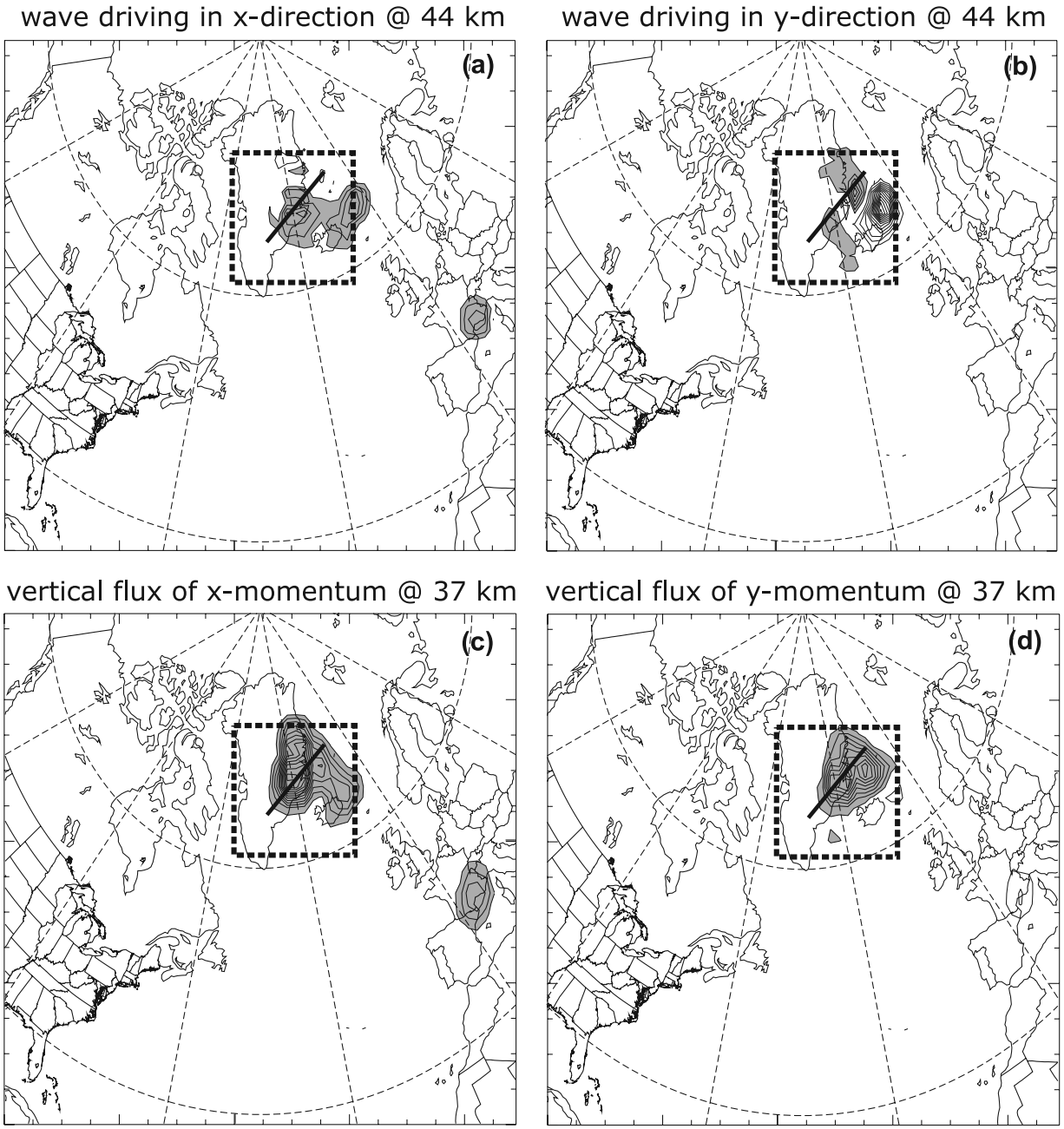

Figure 11. (a) Local wave driving in the x direction (F_x, contoured every 0.1 m s^{-1} hour^{-1}) at 44 km. (b) Same as Figure 11a except in the y direction (F_y). (c) Vertical flux of momentum in the x direction contoured every 5x10^{-3} kg m^{-1} s^{-2} at 37 km. (d) Same as Figure 11c except in the y direction. All negative contours are shaded. The thick line over Eastern Greenland indicates the AB slice and is shown for reference. The rectangular box indicates the region of focus shown in previous figures. All quantities shown are from the simulation at 1200 UTC.

cause additional localized deceleration of the overall flow. The wave influence is particularly evident in the diminished horizontal flow speed shown in AB cross-sections from 1100 to 1700 UTC (Figure 9).

[40] The possible influence of the simulated gravity waves on the upper stratospheric vortex is more quantitatively examined in Figure 11. Here the entire model RM domain is divided into 150- × 150-km subareas (i.e., 10-grid points × 10-grid points squares). Vertical fluxes of momenta in the model's x direction (i.e., $\rho_o\overline{u'w'}$) and the y direction (i.e., $\rho_o\overline{v'w'}$) are computed for each of these areas. The overbar quantity represents a spatial average over each subarea, and the prime indicates the departure from that average. The variables u and v are the horizontal wind components in the model's x and y coordinates; w is the vertical velocity. The computed flux for each subarea is used to represent the value at the center of each subarea box. The resulting central values (smoothed by a two-point running mean) are illus-

trated as contours in Figure 11. Shown in the bottom row, the 1200 UTC fluxes at 2.5 hPa are nearly all negative with maximum amplitudes of 50×10^{-3} kg m^{-1} s^{-2} in the x momentum flux and coincide very well with the wave patterns shown in previous figures.

[41] The vertical convergence of these fluxes (divided by ρ_o) is computed to diagnose the local wave forcing on the horizontal wind in the x and y directions (F_x and F_y, respectively):

$$\left(F_x, F_y\right) = -\frac{1}{\rho_o}\frac{\partial}{\partial z}\left(\rho_o\overline{u'w'}, \rho_o\overline{v'w'}\right).$$

[42] As shown in the top row of Figure 11, the predominant wave forcing tends to occur to the right of the reference AB slice where wave breaking was noted. At 1200 UTC, the magnitude of the deceleration in the x direction (y direction) can reach nearly 0.5 (5) m s^{-1} hour^{-1}. The location of the wave decelerative effects corresponds very well with the depleted wind speed shown in Figure 10 at a slightly later time. This lag correlation (due to the influence of wave driving on wind tendencies) suggests that orographic gravity wave dissipation in the model can interact with the polar vortex by locally slowing down the horizontal flow.

[43] We note that the dissipation mechanism may not be realistic (i.e., too large) in the model. However, the decelerative effects are consistent with the wave forcing related to orographic gravity waves. In their examination of katabatic wind generation of orographic gravity waves over Antarctica polar vortex during winter, *Watanabe et al.* [2006], using a general circulation model, determined the localized deceleration of westerly winds to be greater than 30 m^{-1} s^{-1} day^{-1} in the middle atmosphere because of wave dissipation. This forcing, in turn, exerts notable influence on the horizontal circulation of the polar vortex. Similarly, using satellite data and modeling results, *Eckermann and Preusse* [1999] estimated similar decelerative effects in the Southern Hemisphere upper stratospheric vortex edge due to orographic waves generated by flow over the Southern Andes. In the present study, we estimate the deceleration to be about 12–120 m^{-1} s^{-1}day^{-1}.

[44] We caution that the size of the subarea used in the above calculation does affect the detailed structure and amplitudes of the results shown here. In particular, when the subarea size is increased, the amplitudes shown in Figure 11 weaken and the structure of the contours becomes less detailed, as expected. Regardless, the presented results remain qualitatively unchanged. Furthermore, while the forcings may appear large compared with time-averaged zonal mean gravity wave forcing in global circulation models, this deceleration effect may not be persistent for the entire day and is highly localized in longitude.

4. Summary

[45] The ARPS model is used to simulate gravity waves throughout the troposphere and stratosphere during the case on 24 January 2005 when the stratospheric vortex was very stable and unusually cold. The model generates pronounced gravity wave features over the Eastern Greenland in association with the forcing by Greenland mountainous terrain. Growing in strength and spatial coverage with altitude, wave disturbances over Greenland are dominated by horizontal wavelengths of 80–300 km and vertical wavelengths of 7–20 km. Wind speed reduction in the circumpolar jet occurs downstream of Greenland and is coincident with regions of strong wave forcing because of vertical divergence of the horizontal momentum fluxes as a result of wave breaking. The penetration of these waves into the stratosphere from their near-surface source is fostered by the persistently strong eastward flow that is nearly perpendicular to the Greenland terrain and nearly unidirectional throughout the vertical domain. Thus the present simulation shows that orographic gravity waves interact strongly with the polar vortex by locally slowing down the circumpolar wind. The simulated gravity wave features compare favorably with AIRS radiance perturbations.

[46] To date, details of how gravity waves interact with the stratospheric jet are still unclear. Without proper understanding of gravity waves, our ability to understand present climate and its evolution using chemistry-climate models is tenuous. *Pawson* [1997] suggested that gravity waves can trigger strong wintertime polar vortex disturbances, associated with rapid warming of the polar stratosphere. These warming events can couple with near-surface climate through their influence on the leading mode of climate variability, referred to as the "Annular Modes" [*Baldwin and Dunkerton*, 2001; *Limpasuvan et al.*, 2004, 2005]. Furthermore, breaking gravity waves along the vortex's edge can induce a residual circulation that can substantially warm the Arctic stratopause/upper stratosphere region in the vortex core through adiabatic descent [*Hitchman et al.*, 1989]. The warming over Eureka observed by *Duck et al.* [2000], when the vortex is nearly over the pole, appeared to support this mechanism.

[47] This paper demonstrates the feasibility of ARPS as a tool to improve our understanding of gravity waves. In our case study, we tried to perform a simulation with the most realistic flow conditions throughout the troposphere and the stratosphere in an effort to link the upper stratospheric gravity waves to their possible tropospheric source(s). Moreover, with the enhanced horizontal resolution, we are able to diagnose the effects of gravity waves on the prevailing flow that are difficult to observe because of their scales. In choosing this 24 January 2005 case, our intention was not to completely validate or verify the model. Rather, this case (as mentioned in section 1) is particularly interesting for its large amplitude gravity waves (observed by AIRS) and their occurrence in the presence of an unusually cold vortex. It is obvious that existing mesoscale models (the present model included) cannot perfectly simulate gravity waves. There will always be, for example, inherent assumptions, mathematical/computational constraints including resolution and terrain representation, and other physical parameterizations in the model setup that continually must be dealt with, even if computing resources allow for greater resolution. However, we do believe that the ARPS can be reasonably used to examine gravity waves and help us address the potential impact of gravity wave forcing on the stratospheric dynamics.

[48] Regardless, we note that further validation of the model with local soundings and satellite data is needed to fully gain confidence in the extended ARPS model and in validating fine-scale simulated structures. As recommended

by *Alexander and Barnet* [2006], complementary usage of high-resolution models such as ARPS and satellite observations (like AIRS) is the most likely path toward improving the incorporation of gravity wave influences into global climate models. Similarly, sensitivity studies of the model results will also be important. For example, on the basis of the MM5, *Leutbecher and Volkert* [2000] found that increasing surface friction on the terrain slopes reduces the excited gravity wave amplitudes in the stratosphere and higher model horizontal resolution enhances the amplitude. Further validation and sensitivities studies will be the focus of future work.

[49] **Acknowledgments.** This work was supported by the NASA/South Carolina EPSCoR Program, ASEE/NASA Faculty Fellowship Program, and NSF ATM-0213248 and ATM-0646672. Support for MJA came from NASA contract NNH04CC54C. MX and MH were supported by NSF ATM-0129892 and ATM-0530814. Part of this work was performed at the Jet Propulsion Laboratory, California Institute of Technology, under contract with NASA. The computation for this work was performed at NASA Ames' Columbia Altrix Cluster under the support of NASA Science Mission Directorate (SMD) project Columbia. V.L. particularly thanks (1) Takeshi Horinouchi for providing initial inspiration and assistance in setting up ARPS, (2) Joe W. Waters at NASA JPL for his encouragement during this work, and (3) Marc Michelson at the University of Washington for his computing assistance. Sounding data were provided by Larry Oolman at the University of Wyoming. Finally, we are very grateful to three anonymous reviewers whose suggestions greatly improved the initial manuscript.

References

Alexander, M. J., and C. Barnet (2006), Using satellite observations to constrain parameterizations of gravity wave effects for global models, *J. Atmos. Sci*, in press.

Aumann, H. H., et al. (2003), AIRS/AMSU/HSB on the Aqua mission: Design, science objectives, data products, and processing systems, *IEEE Trans. Geosci. Remote Sens.*, *41*, 253–264.

Baldwin, M. P., and T. J. Dunkerton (2001), Stratospheric harbingers of anomalous weather regimes, *Science*, *294*, 581–584.

Bloom, S., et al. (2005), Documentation and Validation of the Goddard Earth Observing System (GEOS) Data Assimilation System—Version 4, *Technical Report Series on Global Modeling and Data Assimilation 104606*, 26.

Businger, J. A., J. C. Wyngaard, Y. Izumi, and E. F. Bradley (1971), Flux-profile relationships in the atmospheric surface layer, *J. Atmos. Sci.*, *28*, 181–189.

Buss, S., A. Hertzog, C. Hostetler, T. P. Bui, D. Lüthi, and H. Wernli (2004), Analysis of a jet stream induced gravity wave associated with an observed stratospheric ice cloud over Greenland, *Atmos. Chem. Phys.*, *4*, 1183–1200.

Byun, D. W. (1990), On the analytical solutions of flux-profile relationships for the atmospheric surface layer, *J. Appl. Meteorol.*, *29*, 652–657.

Carslaw, K. S., et al. (1998), Increased stratospheric ozone depletion due to mountain-induced atmospheric waves, *Nature*, *391*, 675–678.

Carslaw, K. S., M. Wirth, A. Tsias, B. P. Luo, A. Dörnbrack, M. Leutbecher, H. Volkert, W. Renger, J. T. Bacmeister, and T. Peter (1999), Particle microphysics and chemistry in remotely observed mountain polar stratospheric clouds, *J. Geophys. Res.*, *103*, 5785–5796.

Chou, M.-D., and M. J. Suarez (1994), An efficient thermal infrared radiation parameterization for use in general circulation models, *NASA Tech Memo* 104606, 85 pp.

Chou, M.-D., and M. J. Suarez (1999), A shortwave radiation parameterization for atmospheric studies, 15, NASA/TM-104606, 40 pp.

Chow, F. K., A. P. Weigel, R. L. Street, M. W. Rotach, and M. Xue (2006), High-resolution large-eddy simulations of flow in a steep Alpine valley. Part I: Methodology, verification and sensitivity studies, *J. Appl. Meteor.*, 63–86.

Davies, H. (1983), Limitations of some common lateral boundary schemes used in regional NWP models, *Mon. Weather Rev.*, *111*, 1002–1012.

Deardorff, J. W. (1980), Stratocumulus-capped mixed layers derived from a three-dimensional model, *Boundary Layer Meteorol.*, *18*, 495–527.

Dörnbrack, A., et al. (2002), Evidence for inertial gravity waves forming polar stratospheric clouds over Scandinavia, *J. Geophys. Res.*, *107*(D20), 8287, doi:10.1029/2001JD000452.

Doyle, J. D., et al. (2000), An intercomparison of model-predicted wave breaking for the 11 January 1972 Boulder windstorm, *Mon. Weather Rev.*, *129*, 901–914.

Doyle, J. D., M. A. Shapiro, Q. Jiang, and D. Bartels (2005), Large-amplitude mountain wave breaking over Greenland, *J. Atmos. Sci.*, *62*, 3106–3126.

Duck, T. J., J. A. Whiteway, and A. I. Carswell (2000), A detailed record of High Arctic middle atmospheric temperatures, *J. Geophys. Res.*, *105*(D18), 22,909–22,918, doi:10.1029/2000JD900367.

Dudhia, J. (1993), A nonhydrostatic version of the Penn State-NCAR mesoscale model: Validation tests and simulation of an Atlantic cyclone and cold front, *Mon. Weather Rev.*, *121*, 1493–1513.

Eckermann, S., and P. Preusse (1999), Global measurements of stratospheric mountain waves from space, *Science*, *286*(5444), 1534–1537.

Eckermann, S. D., A. Dörnbrack, S. B. Vosper, H. Flentje, M. J. Mahoney, T. P. Bui, and K. S. Carslaw (2006), Mountain wave-induced polar stratospheric cloud forecasts for aircraft science flights during SOLVE/THESEO 2000, *Wea. Forecasting*, *21*, 42–68.

Fetzer, E., et al. (2003), AIRS/AMSU/HSB validation, *IEEE Trans. Geosci. Remote Sens.*, *41*, 418–431.

Fleming, E. L., S. Chandra, J. J. Barnett, and M. Corney (1990), Zonal mean temperature, pressure, zonal wind, and geopotential height as function of latitude, *Adv. Space Res.*, *10*(Issue 12), 11–59.

Fritts, D. C., and M. J. Alexander (2003), Gravity wave dynamics and effects in the middle atmosphere, *Rev. Geophys.*, *41*(1), 1003, doi:10.1029/2001RG000106.

Gill, A. E. (1982), *Atmosphere-Ocean Dynamics*, 662 pp., Elsevier, New York.

Grell, G., J. Dudhia, and D. Stauffer (1995), A Description of the Fifth-Generation Penn State/NCAR Mesoscale Model (MM5). Mesoscale and Microscale Meteorology Division, NCAR/TN-398+STR, 117 pp.

Hitchman, M. H., J. C. Gille, C. D. Rodgers, and G. Brassuer (1989), The Separated polar winter stratopause: A gravity wave driven climatological feature, *J. Atmos. Sci.*, *46*, 410–422.

Hitchman, M. H., M. L. Buker, G. J. Tripoli, E. V. Browell, W. B. Grant, T. J. McGee, and J. F. Burris (2003), Nonorographic generation of Arctic polar stratospheric clouds during December 1999, *J. Geophys. Res.*, *108*(D5), 8325, doi:10.1029/2001JD001034.

Horinouchi, T., T. Nakamura, and J. Kosaka (2002), Convectively generated mesoscale gravity waves simulated throughout the middle atmosphere, *Geophys. Res. Lett.*, *29*(21), 2007, doi:10.1029/2002GL016069.

Jimenez, C., H. C. Pumphrey, I. A. MacKenzie, G. L. Manney, M. L. Santee, M. J. Schwartz, R. S. Harwood, and J. W. Waters (2006), EOS MLS observations of dehydration in the 2004–2005 polar winters, *Geophys. Res. Lett.*, *33*, L16806, doi:10.1029/2006GL025926.

Kain, J. S., and J. M. Fritsch (1993), Convective parameterization for mesoscale models: The Kain-Fritsch scheme, *The Representation of Cumulus Convection in Numerical Models*, *Meteor. Monogram*, 24, No. 46, *Amer. Meteor. Soc*., 165–170.

Klemp, J. B., and R. B. Wilhelmson (1978), The simulation of three-dimensional convective storm dynamics, *J. Atmos. Sci.*, *35*, 1070–1096.

Leutbecher, M., and H. Volkert (2000), The propagation of mountain waves into the stratosphere: quantitative evaluation of three-dimensional simulations, *J. Atmos. Sci.*, *57*, 3090–3108.

Lilly, D. K., and E. J. Zipser (1972), The Front Range windstorm of 11 January 1972, *Weatherwise*, *25*, 53–56.

Limpasuvan, V., D. W. J. Thompson, and D. L. Hartmann (2004), The life cycle of Northern Hemisphere stratospheric sudden warming, *J. Clim.*, *17*, 2584–2596.

Limpasuvan, V., D. L. Hartmann, D. W. J. Thompson, K. Jeev, and Y. L. Yung (2005), Stratosphere-troposphere evolution during polar vortex intensification, *J. Geophys. Res.*, *110*, D24101, doi:10.1029/2005JD006302.

Lin, Y. L., R. D. Farley, and H. D. Orville (1983), Bulk parameterization of snow field in a cloud model, *J. Clim. Appl. Meteorol.*, *22*, 1065–1092.

Manney, G. L., M. L. Santee, L. Froidevaux, K. Hoppel, N. J. Livesey, and J. W. Waters (2006), EOS MSL observations of ozone loss in the 2004–2005 Arctic Winter, *Geophys. Res. Lett.*, *33*, L04802, doi:10.1029/2005GL024494.

Maturilli, M., and A. Dörnbrack (2006), Polar stratospheric ice cloud above Spitsbergen, *J. Geophys. Res.*, *111*, D18210, doi:10.1029/2005JD006967.

Nappo, C. (2002), *An Introduction to Atmospheric Gravity Waves*, 275 pp., Elsevier, New York.

Noilhan, J., and S. Planton (1989), A simple parameterization of land surface processes for meteorological models, *Mon. Weather Rev.*, *117*, 536–549.

Pawson, S. (1997), Effects of gravity wave drag in the Berlin troposphere-stratosphere-mesosphere GCM, in *Gravity Wave Processes: Their Parameterization in Global Climate Models*, *NATO ASI Ser., Ser. I*, vol. 50, edited by K. Hamilton, pp. 327–336, Springer New York.

Plougonven, R., H. Teitelbaum, and V. Zeitlin (2003), Inertia gravity wave generation by the tropospheric midlatitude jet as given by the Fronts and Atlantic Storm-Track Experiment radio soundings, *J. Geophys. Res.*, *108*(D21), 4686, doi:10.1029/2003JD003535.

Plougonven, R., and C. Snyder (2005), Gravity waves excited by jets: Propagation versus generation, *Geophys. Res. Lett.*, *32*, L18802, doi:10.1029/2005GL023730.

Skamarock, W., and J. B. Klemp (1992), The stability of time-splitting numerical methods for the hydrostatic and nonhydrostatic elastic systems, *Mon. Weather Rev.*, *120*, 2109–2127.

Smith, R. B. (1979), The influence of mountains on the atmosphere, *Adv. Geophys.*, *21*, 87–230.

Tao, W.-K., et al. (2003), Microphysics, radiation and surface processes in the Goddard Cumulus Ensemble (GCE) model, *Meteorol. Atmos. Phys.*, *82*, 97–137.

Watanabe, S., K. Sato, and M. Takahashi (2006), A general circulation model study of the orographic gravity waves over Antarctica excited by katabatic winds, *J. Geophys. Res.*, *111*, D18104, doi:10.1029/2005JD006851.

Wu, D. L., and F. Zhang (2004), A study of mesoscale gravity waves over the North Atlantic with satellite observations and a mesoscale model, *J. Geophys. Res.*, *109*, D22104, doi:10.1029/2004JD005090.

Xue, M., and A. J. Thorpe (1991), A mesoscale numerical model using the nonhydrostatic pressure-based sigma coordinate equations: model experiments with dry mountain flows, *Mon. Weather Rev.*, *119*, 1168–1185.

Xue, M., K. K. Droegemeier, and V. Wong (2000), The Advanced Regional Prediction System (ARPS)—A multiscale nonhydrostatic atmospheric simulation and prediction tool. Part I: Model dynamics and verification, *Meteorol. Atmos. Phys.*, *75*, 161–193.

Xue, M., K. K. Droegemeier, V. Wong, A. Shapiro, K. Brewster, F. Carr, D. Weber, Y. Liu, and D.-H. Wang (2001), The Advanced Regional Prediction System (ARPS)—A multiscale nonhydrostatic atmospheric simulation and prediction tool: Part II. Model physics and applications, *Meteorol. Atmos. Phys.*, *76*, 143–165.

Xue, M., D. Wang, J. Gao, and K. K. Droegemeier (2003), The Advanced Regional Prediction System (ARPS), storm-scale numerical weather predication and data assimilation, *Meteorol. Atmos. Phys.*, *82*, 130–170, doi:10.1007/s00703-001-0595-6.

M. Hu and M. Xue, Center for Analysis and Prediction of Storms, University of Oklahoma, Norman, OK, USA.

M. Joan Alexander, Colorado Research Associate Division, NorthWest Research Associates, Inc., Boulder, CO, USA.

V. Limpasuvan, Department of Chemistry and Physics, Coastal Carolina University, P.O. Box 261954, Conway, SC 29528, USA. (var@coastal.edu)

S. Pawson, Global Modeling and Assimilation Office, NASA Goddard Space Flight Center, Greenbelt, MD, USA.

J. R. Perkins, Department of Computer Sciences, Coastal Carolina University, Conway, SC, USA.

D. L. Wu, NASA Jet Propulsion Laboratory, California Institute of Technology, Pasadena, CA, USA.